PNAS
www.pnas.org

Supplementary Information for:

Structural Bases for F Plasmid Conjugation and F Pilus Biogenesis in *Escherichia coli*

Bo Hu*, Pratick Khara, and Peter J. Christie*

Department of Microbiology and Molecular Genetics, McGovern Medical School,

6431 Fannin St, Houston, Texas 77030

*Correspondence to: Bo Hu or Peter J. Christie

Department of Microbiology and Molecular Genetics, McGovern Medical School, Houston, TX 77030.

Fax: 713-500-5499

Hu:
Phone: 713-500-5891
e-mail: Bo.Hu@uth.tmc.edu

Christie:
Phone: 713-500-5440
e-mail: Peter.J.Christie@uth.tmc.edu

This PDF file includes:
Supplementary Text: Materials and Methods
Tables S1, S2
Figures S1-S8
References 1-23

Other supplementary materials for this manuscript include the following:
Movies S1, S2

Materials and Methods

Strain constructions: pED208 *tra* genes were deleted by substitution with antibiotic resistance gene cassettes using standard recombineering procedures (1). Nonpolar effects of the *tra* gene mutations were confirmed by complementation with the corresponding *tra* gene expressed from the P_{BAD} promoter.

Mating assay. Donor and recipient cells were grown overnight in presence of the appropriate antibiotics, diluted 1:1,000 in fresh antibiotic-free LB media, and incubated with shaking for 1.5 h. If necessary, cells were induced with arabinose (0.2 % final concentration) and incubated with shaking for an additional 1.5 h. Equal volumes of donor and recipient cell cultures were mixed and incubated with shaking for 3 h. Mating mixtures were serially diluted and plated onto LB agar containing antibiotics selective for transconjugants (Tc's) and donors. The frequency of DNA transfer was calculated as the number of Tc's per donor (TCs/D). To assess the donor potential of minicells, a 10 ml culture of the minicell-producing strain UU2834(pED208) was grown to mid-exponential phase (OD_{600} 0.5) and minicells were purified by differential centrifugation and passage through a 0.45 μm filter (2). Minicells devoid of viable donors were deposited onto nitrocellulose filter discs and incubated with recipient cells for 3 h at 37°C. Discs were suspended in LB, serially diluted and plated on LB agar containing antibiotics selective for Tc's, recipients, and donors (to confirm the absence of viable donor cells).

Phage infection. Overnight grown cells (30 μl) were plated on LB-agar supplemented with antibiotics and 0.2% arabinose when necessary. After drying, the plates were spotted with 2 μl of M13 phage (titer of 10^{11} phage/ml) and incubated overnight at 37°C. Plaque formation served as an indicator of F pilus production (3).

Cohesion assay. F pilus-mediated aggregation of *E. coli* strains was assessed with a cohesion assay. Briefly, cells were grown overnight at 37°C, then subcultured by dilution (1:1,000) in fresh LB media and further incubation with shaking for 3.5 h at 37°C. Cultures (1 ml) were placed in a cuvette and clearance of the culture due to F pilus-mediated aggregation of cells was monitored spectrophotometrically, with OD_{600} readings at 30 min intervals or at the end of a 3 hr time period. A cohesion index for each strain was calculated relative to that determined for the isogenic, plasmid-free strain MC4100 (set to a value of 1).

Western Blotting Steady-state levels of TraC, TraC.K487Q, and TraC-sfGFP, each with Strep epitope tags at their C-termini, were determined by western blot analyses. Cell lysates from strains producing the proteins of interest were loaded on an SDS-polyacrylamide gel on a per cell equivalent basis prior to electrophoresis, western transfer, and immunostaining with anti-Strep antibodies. As a loading control, blots were developed with antibodies against the β-subunit of *E. coli* RNA polymerase.

Transmission electron microscopy. Strains were grown overnight at 37°C on an LB agar plate supplemented with spectinomycin. A loopful of cells was collected and resuspended in 500 -1,000 μl PBS using a cut pipette tip. The cell suspension (7 μl) was placed on the shiny side of a Formvar/Carbon Film 200 Mesh Nickel grid (Electron Microscopy Sciences FCF200-NI) for 1 min. The grid was washed 5 times with H_2O. Uranyl acetate (7 μl, 1% solution depleted of uranium; EMS) was applied to the grid for 1 min and then removed by wicking with a tissue. The grid was imaged using a JEOL JEM-1400 microscope equipped with a Gatan camera.

Cryo-ET Data Collection and 3-D Reconstructions. The frozen-hydrated specimens were imaged at −170 °C using a Polara G2 electron microscope (FEI Company) equipped with a field emission gun and a direct detection device (Gatan K2 Summit). The microscope was operated at 300 kV with a magnification of ×15,500, resulting in an effective pixel size of 2.5 Å at the specimen level. We used SerialEM (4) to collect low-dose, single-axis tilt series with dose fractionation mode at about 5 μm defocus. Tilt series were collected from -51° to 51° with increment of 3° and a cumulative dose of ~60 $e^-/Å^2$ distributed over 35 stacks. Each stack contains ~8 images. We used Tomoauto (5) to facilitate data processing which includes drift correction of dose-fractionated data

using Motioncorr (6) and assembly of corrected sums into tilt series, automatic fiducial seed model generation, alignment and contrast transfer function correction of tilt series by IMOD (7), and reconstruction of tilt series into tomograms by Tomo3D (8). Each tomographic reconstruction is 3,710 × 3,838 × 2,400 pixels and ~130 Gb in size. In total, 1,309 tomographic reconstructions from 6 different strains were generated.

Sub-tomogram averaging and correspondence analysis. We used tomographic package I3 for sub-tomogram analysis as described previously (9). A total of 3,811 F1-CH, 365 F2-CH/Pilus and 1,800 F3-ST/Pilus secretion machines (400 × 400 × 400 voxels) were visually identified and then extracted from 1309 cryo-tomographic reconstructions (Table S2). Two of the three Euler angles of each secretion machine were estimated based on the orientation of each particle in the cell envelope. To accelerate image analysis, 4×4×4 binned sub-tomograms (100×100×100 voxels) were used for initial alignment. The alignment proceeds iteratively with each iteration consisting of three parts in which references and classification masks are generated, sub-tomograms are aligned and classified, and finally class averages are aligned to each other. Classification focusing on core complex showed a 13-fold symmetry feature, so in the following processing 13-fold symmetry was imposed to assist the sub-tomograms alignment. Classification focusing on the IMC showed a 6-fold symmetry feature, and in the following processing 6-fold symmetry was imposed to assist in sub-tomograms alignment. After multiple cycles of alignment and classification for 4×4×4 binned sub-tomograms, we used 2×2×2 binned sub-tomograms for refinement. Fourier shell correlation (FSC) between the two independent reconstructions was used to estimate the resolution of the averaged structures (see *SI Appendix,* Fig. S3C). FSC was also used to estimate resolutions of IMC or OMC structures for the F2-CH/P and F3-ST/P structures or mutant machines characterized in this study (see *SI Appendix,* Fig. S3D).

3-D Visualization and Molecular Modeling. We used IMOD to visualize the maps and also to generate 3-D surface rendering of *E. coli* minicells and UCSF Chimera (10) to visualize subtomogram averages in 3-D and molecular modeling.

Table S1. List of bacterial strains, plasmids, and oligonucleotides used in this study.

Strain	**Genotype or description**	**Source**
MC4100-RifR	F- *[araD139]$_{B/r}$* Δ(*argF-lac*)*169* λ$^-$ *e14*$^-$ *flhD5301* Δ(*fruK-yeiR*)*725*(*fruA25*) *relA1 rpsL150*(*strR*) *rbsR22* Δ(*fimB-fimE*)*632(::IS1) deoC1 rifR*	Lab stock
HME45-RifR	W3110 *gal490 pgl*Δ8 λ*c*I*857* Δ*(cro-bioA) rifR*	Lab stock
UU2834	*(tsr)5547 (aer)1 ygjG::genR (trg)4543 min::kan (flbB-flaH)4 mreB-A125V thr(Am)-1 leuB6 his-4 metF(Am)159 rpsL136 [thi-1 ara-14 lacY1 mtl-1 xyl-5 tonA31 tsx-78]*	Parkinson JS
MG1655	K-12 F$^-$ λ$^-$ *ilvG*$^-$ *rfb-50 rph-1*	Lab stock
WM5351	MG1655-Δ*thrC::kanR*	(11)
GL38	MG1655-Δ*aer*::*sfGFP kanR*	(12)
TUC01	HME45::*sacB catR*	(13)
DH5α	F$^-$ *endA1 glnV44 thi-1 recA1 relA1 gyrA96 deoR nupG purB20* φ80d*lacZ*ΔM15 Δ(*lacZYA-argF*)U169, hsdR17($r_K^- m_K^+$), λ$^-$	Lab stock
Plasmid	**Relevant characteristics**	**Source**
pBAD24	CrbR, P_{BAD} cloning vector	This study
pBAD33	ChlR, P_{BAD} cloning vector	This study
pCDFDuet-1	SpcR, CloDF13 *ori*, *lacI*, *T7lac*	Novagen, Madison, WI
pOX38	TetR, 1-3 F pili per cell	(14)
pED208	*lac*$^+$, high-frequency transfer, hyperpiliated	(15)
pED208-Spc	SpcR variant	This study
pED208-Spc Δ*traA*	SpcR, pED208 deleted of *traA*	This study
pED208-Spc Δ*traD*	SpcR, pED208 deleted of *traD*	This study
pED208-Spc Δ*traB*	SpcR, pED208 deleted of *traB*	This study
pED208-Chl Δ*traC*	ChlR, pED208 deleted of *traC*	This study
pPK15	CrbR, pBAD24 expressing *traC*	This study
pPK17	CrbR, pBAD24 expressing *traA*	This study
pPK18	CrbR, pBAD24 expressing *traD*	This study
pPK19	CrbR, pBAD24 expressing *traB*	This study
pPK25	CrbR, pBAD24 expressing *traC-sfGFP*	This study
pPK32	CrbR, pBAD24 expressing *traC-Strep*	This study
pPK33	CrbR, pBAD24 expressing *traC-sfGFP-Strep*	This study
pPK35	CrbR, pBAD24 expressing *traC.K487Q-Strep*	This study

Primer	**Sequence (5' to 3')**	**Purpose**
deltraC-pCm_F2	CCGACTGGGTTCTTCCGGCCAGGGTAAATTAA GGAGTTTCGGTGATCGGCACGTAAGAGGTTCC	*traC* deletion
deltraC-Cm_R1	CCCCCTTTGAACTGAACATCGCGCGACTGAGC GGATCGACAAATTACGCCCCGCCCTGC	*traC* deletion
traC-NheI_F	CTAGCTAGCAGGAGGAATTCACCGTGAAAAA	*traC* cloning

	ATTTCTGAACGTACTGGAAAATCTG	
traC-HindIII_R	CCCAAGCTTTTTTTGGTCAGTGGTCATGCAGC	*traC* cloning
pED208-traC_F	GTCGGCAAATTTGATGAGCTGC	Δ*traC* sequence confirmation
pED208-traC_R	AAAACAGATCTATGCCATTCTTCTTGAAGG	Δ*traC* sequence confirmation
pED208-up_traC_F	TGTAAACACAAACACGACAACGTCAAC	Δ*traC* sequence confirmation
pED208-dn_traC_R	CTGGTCATAAATCGTTCGGTAAGAGCC	Δ*traC* sequence confirmation
pSp_F	CCTGTCTTTACTGTTGCTTCAATCAAACAAAAGGAATTCACTTCAAATATGTATCCGCTCATGAGACAATAAC	Spc^r cassette insertion in pED208
pSp_R	GTTTGCCTTTATCACTTCCGCCAGAATCTGTCGCAGAAGCACGTTATTTGCCGACTACCTTGGTGATCTC	Spc^r cassette insertion in pED208
traX-end_F	TGCTTTCCGGCGTGATTCTTAC	pED208-Spc sequence confirmation
traX-end_R	AAGCTTTGTTCCCCTCGCTCC	pED208-Spc sequence confirmation
pED208-deltraA-sacCm_F	CCCGTCAATACCGCTGGGTGTTAATTGAAATAGCATAAATGGAGTTTTTATCAAAGGGAAAACTGTCCATAT	*traA* deletion
pED208-deltraA-sacCm_R	CTGACAGGGTTTTCGGGAAACGGTATTTGTCTAAATCGTTTCCCTCCATATGTGACGGAAGATCACTTCG	*traA* deletion
pED208-up-traA_F	AAGCTGAATTAAGACTGGAGGATCATTTACG	Δ*traA* sequence confirmation
pED208-dn-traA_R	ATACCAATAACACCAGTTGTATAACCAGCG	Δ*traA* sequence confirmation
traA-NheI_F	CTAGCTAGCAGGAGGAATTCACCATGAATTTATCCTTTGCAAAAGGCG	*traA* cloning
traA-HindIII_R	CCCAAGCTTTCATTTGATGAAGGTAAGACCGACG	*traA* cloning
pED208-deltraD-sacCm_F	CAGGCCTGTATCCGGCATGTCTGCTGGTTACCTGCTTCCGGGAAAATATAATCAAAGGGAAAACTGTCCATAT	*traD* deletion
pED208-deltraD-sacCm_R	GTTAATGTTGACCTCTTCCCTGCGGGTCATATCGCGGGTCTGGTGTGAGTTCTGTGACGGAAGATCACTTCG	*traD* deletion
pED208-up-traD_F	TTAACCTGAAATTCGAAGAAGCAAAACC	Δ*traD* sequence confirmation
pED208-dn-traD_R	ATCCAGCGGGAATCCAGTGAAC	Δ*traD* sequence confirmation
traD-NheI_F	CTAGCTAGCAGGAGGAATTCACCATGAGCCTGAATCCTCGCGACT	*traD* cloning
traD-HindIII_R	CCCAAGCTTCATCAGTATTCCCTCCCGTCATCC	*traD* cloning

traD_F1	GCTGAAAAAACGCGGAGAAGC	Δ*traD* sequence confirmation
traD_R1	AATATCTCTGCGGCCCCTTTC	Δ*traD* sequence confirmation

pED208-deltraB-sacCm_F	GTTATCCGTGGAAACGGGGAGGGTGAAGATGGCCAACGTTAATAAAGTCGTCATCAAAGGGAAAACTGTCCATAT	*traB* deletion
pED208-deltraB-sacCm_R	GGGCACTAACTATTCCGGATTGTGTTGTTGTGGTCGGTTTCCCGGCCCCGTTGTGACGGAAGATCACTTCG	*traB* deletion
pED208-up-traB_F	CGTTATGAACTGCGTAATGCCAATACC	Δ*traB* sequence confirmation
pED208-dn-traB_R	GCCACAGCTTTCACACTCACTGAG	Δ*traB* sequence confirmation
traB-NheI_F	CTAGCTAGCAGGAGGAATTCACCATGGCCAACGTTAATAAAGTCGTCC	*traB* cloning
traB-HindIII_R	CCCAAGCTTTTACTGTGTGACGACCTGTCCG	*traB* cloning
ipBAD_HindIII_F	CCCAAGCTTGGCTGTTTTGGCGGATGAGAG	Construction of *traC-sfGFP*
i_traC(pED208)_XbaI_R	GCTCTAGATGCAGCCTCCGCAAGCGCTTCAAG	Construction of *traC-sfGFP*
sfGFP-XbaI_F2	GCTCTAGAATGAGCAAAGGAGAAGAACTTTTCACTG	Construction of *traC-sfGFP*
sfGFP-HindIII_R1	CCCAAGCTTTTATTTGTAGAGCTCATCCATGCCATG	Construction of *traC-sfGFP*
ipBAD_Strep_F	phos-CTCAATTCGAAAAGTGAAAGCTTGGCTGTTTTGGCGGATGAGAG	Constuction of *traC-Strep* and *traC-sfGFP-Strep*
itraC(pED208)_Strep_R	phos-GATGAGACCATGCAGCCTCCGCAAGCGCTTCAA	Constuction of *traC-Strep*
itraC-sfGFP(pED208)_Strep_R	phos-GATGAGACCATTTGTAGAGCTCATCCATGGCCATGTGTAATC	Constuction of *traC-sfGFP-Strep*
traC_K487Q_F	phos-GGCCAGACTGGTCTGGTCCAG	*traC.K487Q* cloning
traC_del_R	phos-TGCCCCCGAGGTGCCGGTGA	*traC.K487Q* cloning

Table S2 Cryo-ET data used in this study

No.	Plasmid	Structure	# of tomographic reconstructions	# of Sub-tomograms
1	pED208	F1-CH	511	1,490
2	pED208	F2-CH/Pilus	511	365
3	pED208	F3-ST/Pilus	511	1,800
4	pED208Δ*traA*	F1-CH	166	288
5	pED208Δ*traD*	F1-CH	106	361
6	pED208Δ*traC*	F1-CH	104	348
7	pED208Δ*traC*(TraC.K487Q)	F1-CH	142	531
8	pED208Δ*traC*(TraC-sfGFP)	F1-CH	280	793

Supplementary Figures 1 - 8.

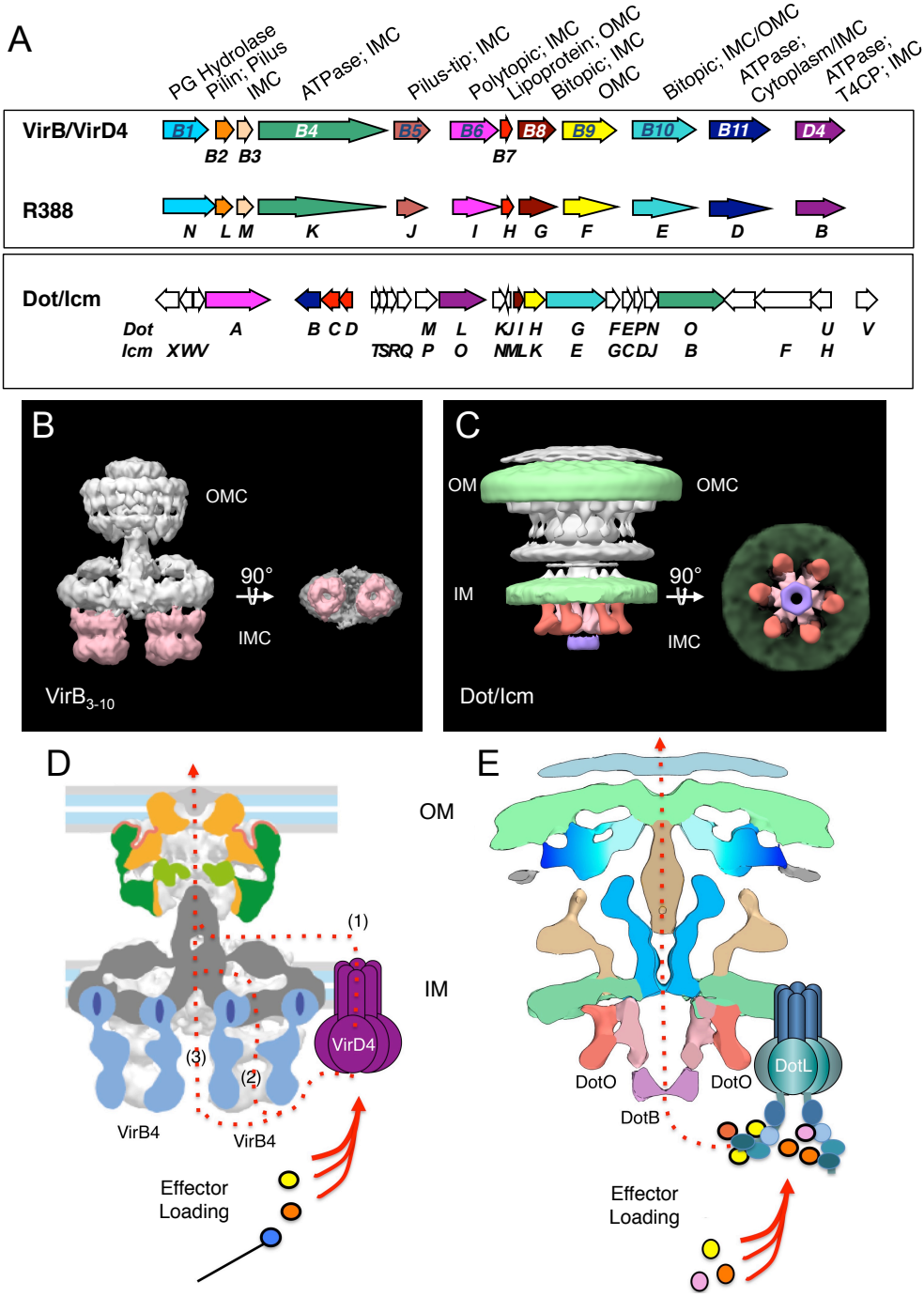

Fig. S1. Structures of T4SSs solved to date. A) Operon arrangements of type IV secretion systems (T4SSs) structurally analyzed to date. The VirB/VirD4 and R388-encoded T4SSs are representatives of 'minimized' T4SSs in Gram-negative species. These systems are assembled from T4SS signature subunits including the 11 VirB subunits and the VirD4 substrate receptor or type IV coupling protein (T4CP). Functions and positional assignments of machine subunits in the encoded T4SS are depicted at the top. The *L. pneumophila* Dot/Icm

system is assembled from signature subunits (color-coded) plus 15 or more system-specific subunits (no shading). **B**) Side and bottom views at 90^{o} angles of the $VirB_{3-10}$ substructure, isolated from the R388 system and reconstructed by single-particle negative-stain electron microscopy (EMD-2567), showing the two side-by-side hexameric barrels of the VirB4 ATPase (pink-shaded). **C)** Side and bottom views at 90^{o} angles of the *L. pneumophila* Dot/Icm machine obtained by *in situ* CryoET (EMD-7611, EMD-7612) showing the central hexamer of dimers of VirB4-like DotO (pink-shaded) and docked VirB11-like DotB (purple-shaded). **D and E)** Schematics comparing the architectures of the R388-encoded conjugation machine and *L. pneumophila* Dot/Icm system and the postulated routes of substrate translocation. In the 'minimized' R388 system, the VirD4 substrate receptor recruits DNA substrates to the T4SS and coordinates with VirB11 and VirB4 ATPases to deliver DNA cargoes through one of 3 possible routes across the cytoplasmic membrane. No central channel has been visualized in this machine (16). In the Dot/Icm system, the VirD4-like DotL receptor recruits effector protein substrates and coordinates with the VirB11-like DotB and VirB4-like DotO ATPases to deliver protein cargoes through the visualized central channel (17).

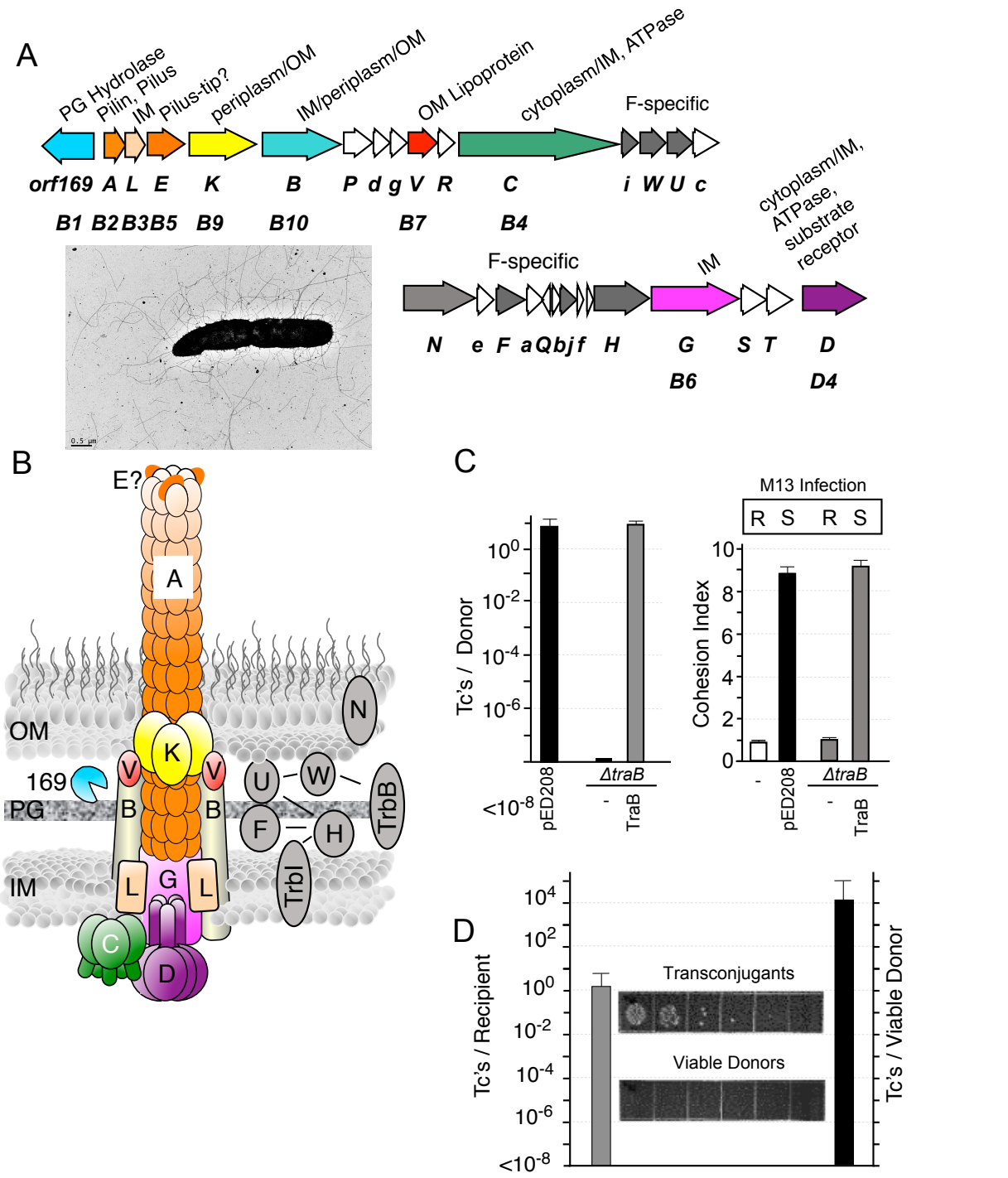

Fig. S2. Phenotypes of strains and minicells harboring pED208 variants. **A)** Schematic of the pED208 *tra* operon, and subcellular localizations and functions of encoded Tra subunits. The F-encoded systems are assembled from homologs of the VirB/VirD4 signature subunits (color coding matches Fig. S1) and ~6-8 Tra subunits specific to F systems (gray-shaded). Unshaded genes encode subunits that do not contribute to machine assembly or whose functions are not characterized. IM, inner membrane; OM, outer membrane; PG, peptidoglycan. The *mreB, minC* mutant strain UU2834(pED208) grows as skinny cells with abundant pili, as visualized by transmission electron microscopy, and also produces abundant, small (<300 nm) minicells.

B) Architecture of the F transfer system, as deduced from defined subcellular locations of Tra subunits and Tra protein interaction networks (18, 19). Conserved Tra subunits are color-matched with *tra* genes presented in panel A; Tra subunits specific to F systems are gray-shaded. F-specific subunits form an interaction network distinct from the VirB/VirD4-like signature subunits, but are required for biogenesis of the translocation channel and F pilus (20). **C)** Left: Transfer frequencies of MC4100 strains harboring pED208, pED208Δ*traB* (*traB* encodes the essential VirB10-like scaffold subunit) (19, 21), or pED208Δ*traB* and the *traB* expression plasmid pPK19. Transfer frequencies are presented as transconjugants (Tc's)/donor. Experiments were repeated at least three times, with median values presented along with standard errors. Right: F-pilus-mediated aggregation was monitored spectrophotometrically to generate a cohesion index value, as described in Materials and Methods. Cohesion indices are presented relative to the plasmid-free strain MC4100 (normalized to 1). Production of F pili was also monitored by susceptibility of cells to infection by the pilus-binding phage M13. R, resistant; S, sensitive. **D)** Minicells from strain UU2834(pED208) function as donors when mated with a viable recipient strain. Minicells devoid of viable donor cells (inset) were mated with recipient cells for 15 min on LB plates. The gray bar at the left denotes transconjugants per recipient cell (Tc's/Recipient). The black bar at the right denotes transfer frequencies of minicell preparations concentrated 10,000 fold. These concentrated minicell preparations had some viable donor cells, but transfer frequencies by these preparations greatly exceeds levels attributable to the viable donor population.

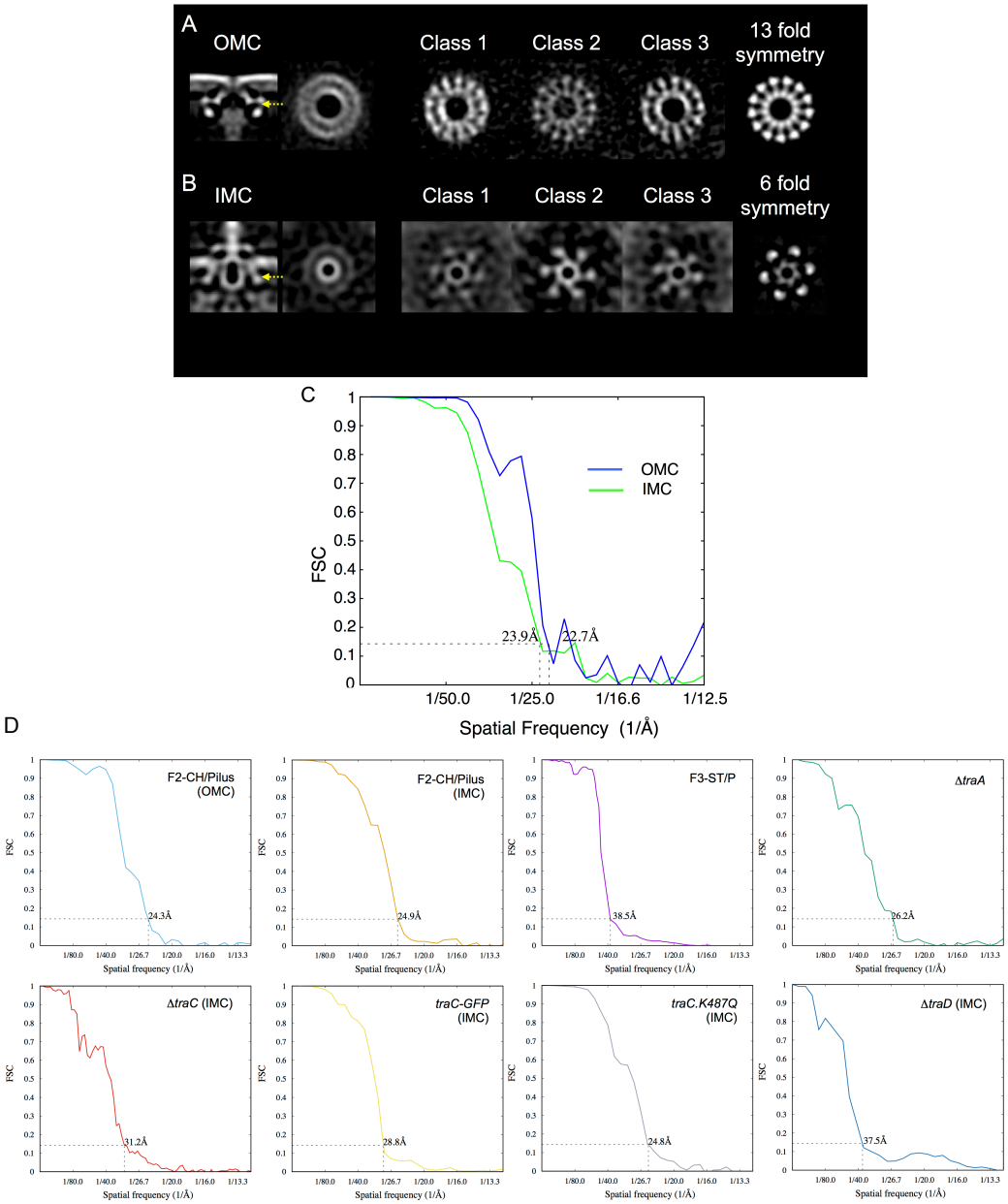

Fig. S3. 3-D classifications reveal 13-fold symmetric features of the F1-CH outer membrane complex (OMC) and 6-fold symmetric features of the inner membrane complex (IMC). For both the OMC and IMC**,** after the initial alignments, multivariate statistical analysis and hierarchical ascendant classification were used to generate at least three class averages. **A)** F1-CH structure: A central section of the OMC and cross section view of the 3D average from the initial alignment. The cross-sections from the OMC of three class averages show 13-fold symmetries, which is clearly evident when 13-symmetry is imposed during refinement (far right). **B)** F1-CH structure: A central section of the IMC and cross section view of the 3D average from the initial alignment. The cross-sections from the IMC of three class averages show 6-fold symmetries, which is more evident when 6-symmetry is imposed during refinement (far right). **C)** Fourier shell correlation plot of sub-volume averages aligned on the F1-CH OMC (blue) and IMC (green) regions. **D)** Fourier shell correlation plots of sub-volume averages for OMCs or IMCs of the F2-CH/Pilus and F3-ST/Pilus structures, and the Δ*tra* mutant machines shown.

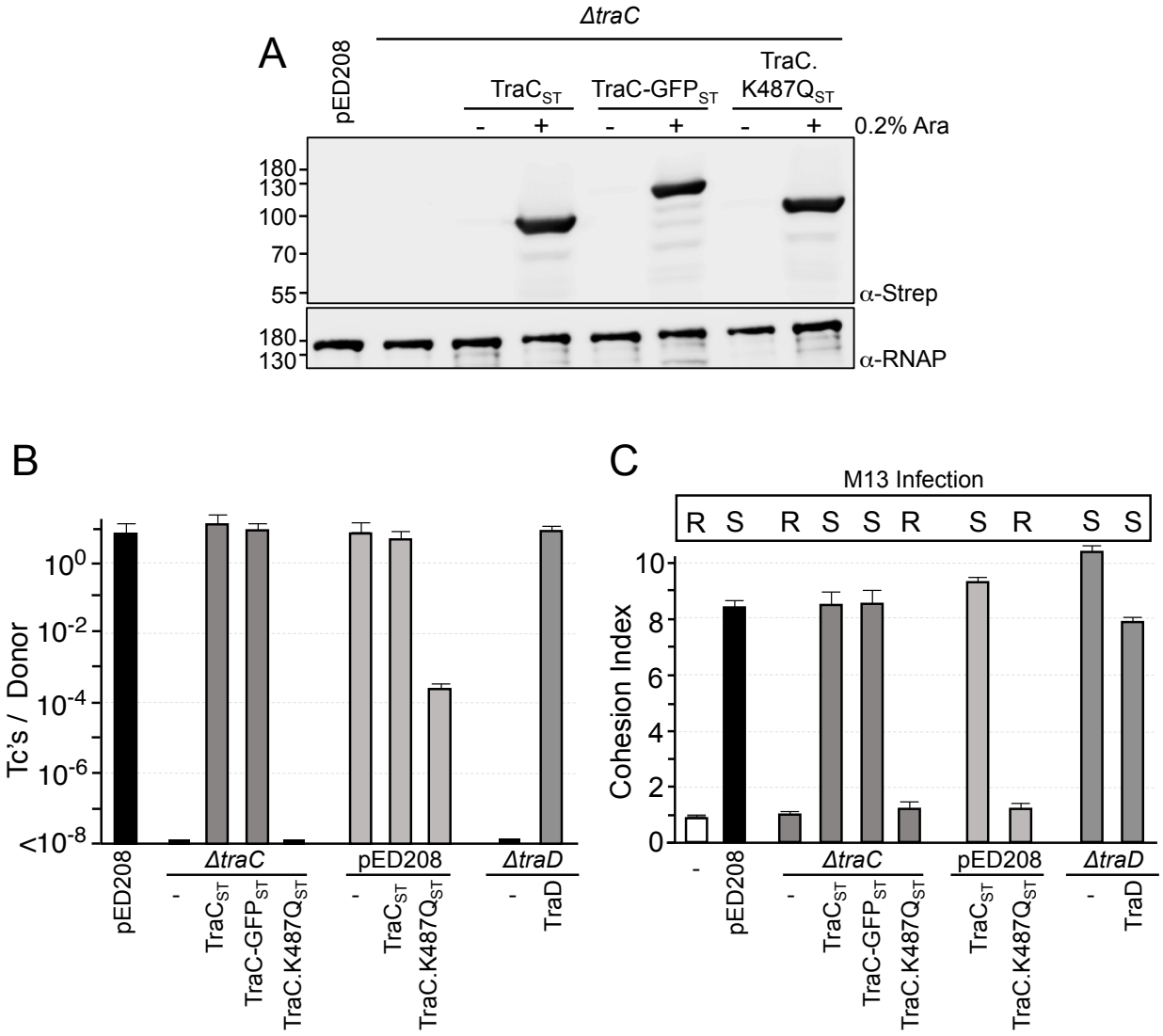

Fig. S4. Phenotypes of strains harboring *traC* and *traD* mutant plasmids. **A)** Abundances of Strep-tagged TraC, TraC-GFP, and TraC.K487Q when produced from the arabinose (Ara)-inducible P_{BAD} promoter, as assessed by immunoblot analysis using anti-Strep antibodies (α-Strep). As a loading control, western blots were developed with antibodies to the β-subunit of RNA polymerase (α-RNAP). **B)** Transfer frequencies of MC4100 harboring pED208 or the Δ*traC* or Δ*traD* mutant plasmids without or with complementing plasmids producing the proteins indicated. Transfer frequencies are presented as Transconjugants (Tc's)/Donor. Experiments were repeated at least three times, with median values presented along with standard errors. **C)** F-pilus mediated aggregation of cells was monitored spectrophotometrically to generate a cohesion index value as described in Materials and Methods. Cohesion indices are presented relative to the plasmid-free strain MC4100 (normalized to 1). F-pilus production was also assessed by sensitivity (S) or resistance (R) to infection by the pilus-binding phage M13.

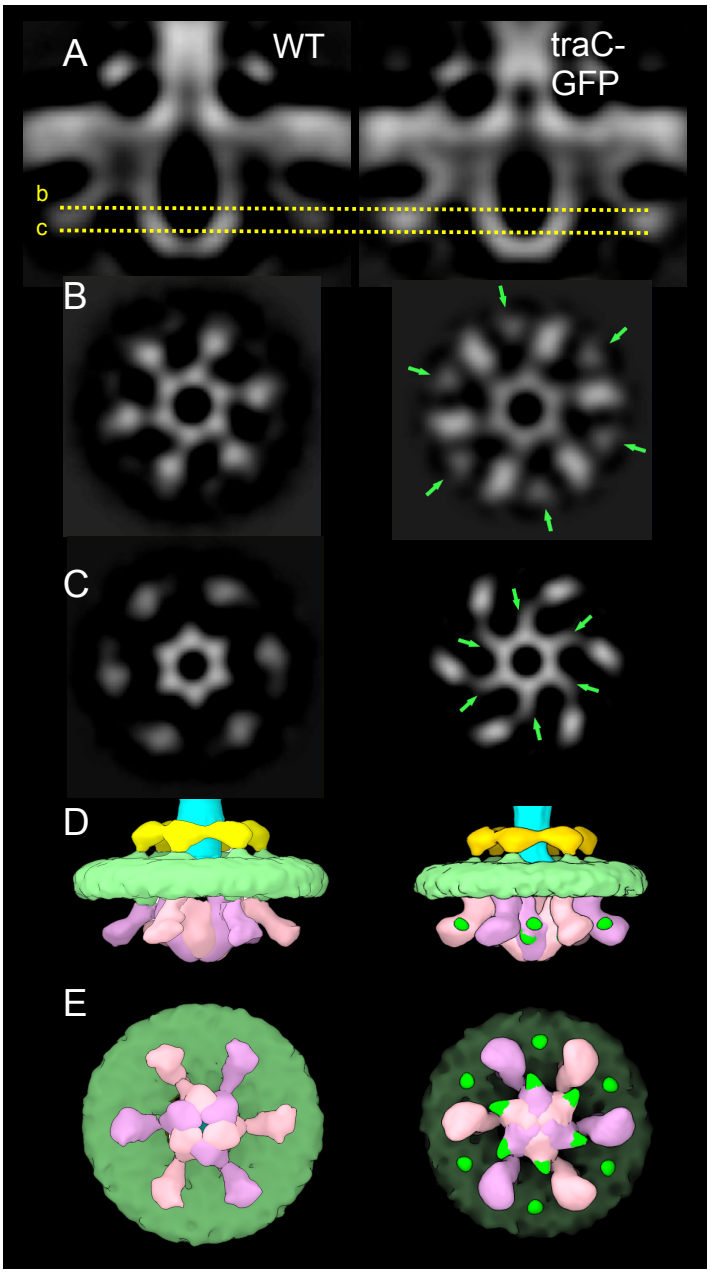

Fig. S5. Comparisons of IMC structures associated with the WT machine and a TraC-GFP mutant machine. (A) Central slices of the averaged IMC structures from the WT machine elaborated by UU2834(pED208) and the TraC-GFP machine elaborated by UU2834(pED208Δ*traC*, pPK25). (B, C) Cross-section views at the positions shown in yellow lines in panel A. Densities corresponding to GFP are indicated by the green arrows. (D, E) Surface renderings showing the IMC collar (yellow), IM (light green), TraC hexamer of dimers (pink), and 12 associated GFP densities (dark green). GFP densities were more distantly located from the outer vs inner arms of the TraC dimer pairs, which we attribute to a combination of the presence of a peptide linker between TraC and GFP and different spatial constraints imposed by packing environments near the outer vs inner arms.

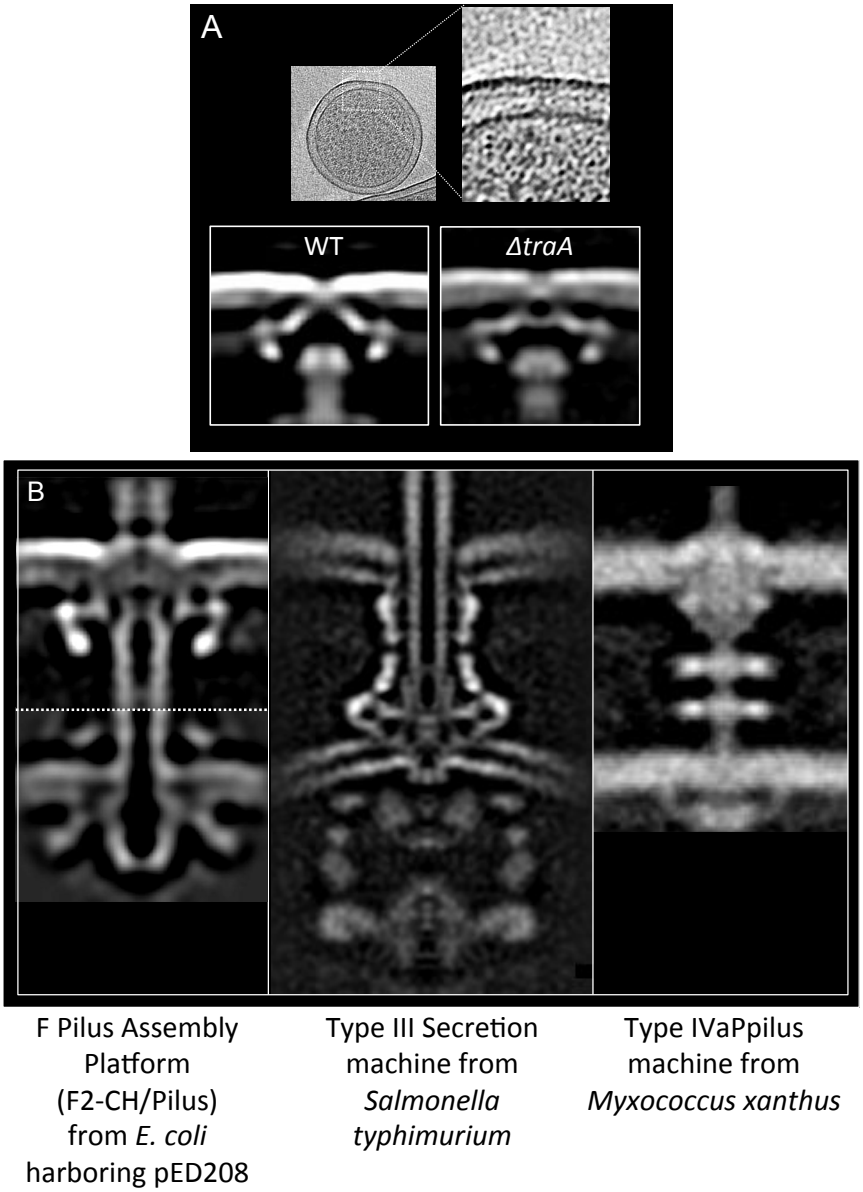

Fig. S6. Evidence for assembly of the F pilus on an outer membrane platform. A) *In situ* structure of the F1-CH complex produced by UU2834(pED208Δ*traA*), a strain lacking the TraA pilin subunit. Upper, a tomographic slice showing an F1-CH complex in a Δ*traA* minicell and corresponding zoomed-in view. Lower, a central slice from global averages shows highly-conserved symmetric features of the OMC and central cylinder in the F1-CH complexes from the WT and Δ*traA* mutant machines, establishing that the OMC and central cylinder are not composed of pilin subunits. **B)** The F2-CH/Pilus complex compared with a type III secretion system (T3SS) and type IV pilus assembly machine. In the F2-CH/Pilus complex, the walls of the F pilus narrow at the junction with the outer membrane-spanning disc and plug domains. The central cylinder extends to the outer membrane where the channel walls pinch together. This overall architecture is consistent with assembly from an outer membrane platform, as opposed to an inner membrane platform as shown for the needle complex elaborated by a *Salmonella typhimurium* T3SS (EMD8544) (22) and a type IV pilus system elaborated by *Myxococcus xanthus* (EMD3247) (23).

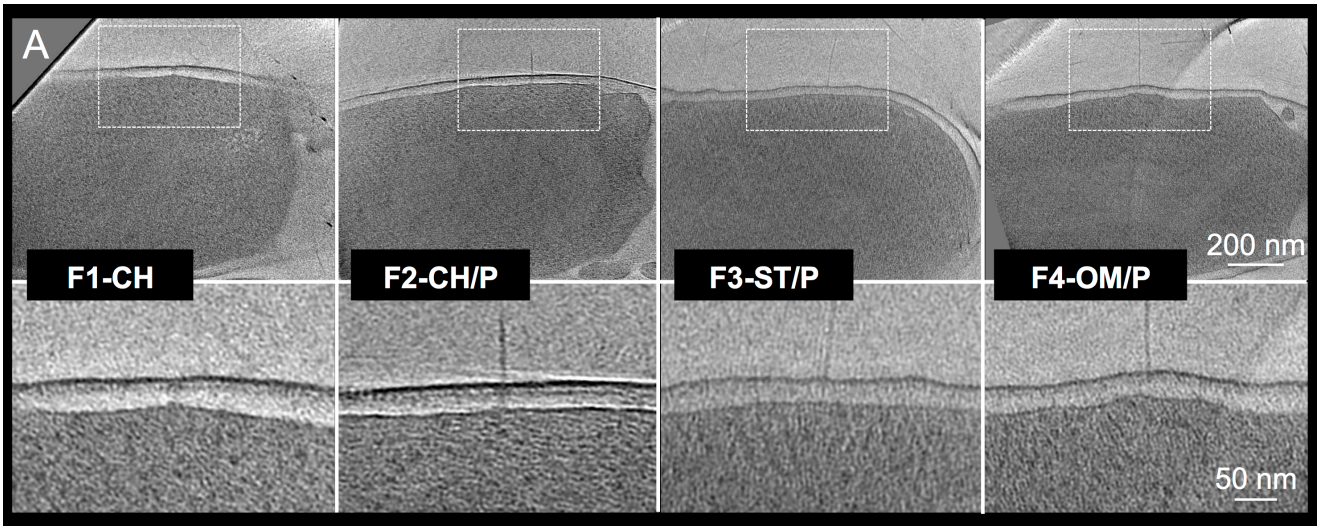

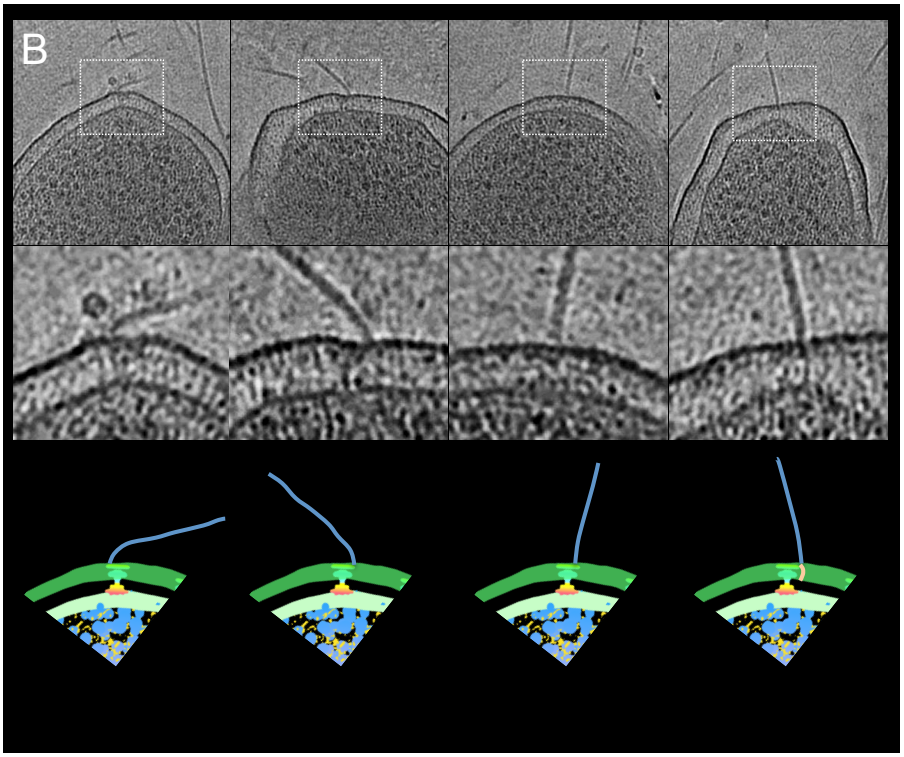

Fig. S7. Structures of F-pilus basal structures. A) F-encoded structures visualized in intact *E. coli* cells. Intact UU2834 cells possess each of the 4 structures visualized in minicells from the same strain. **B)** Slices of F2-CH/Pilus complexes visualized in minicells showing the F pilus positioned asymmetrically on, or near but not physically joined to, the basal structure. Right: Clustering of F1-like basal structures and F3-ST/Pilus complexes. We propose that these variant structures correspond to transition intermediates in the pathways leading to assembly of F3-ST/Pilus and F4-OM/Pilus complexes.

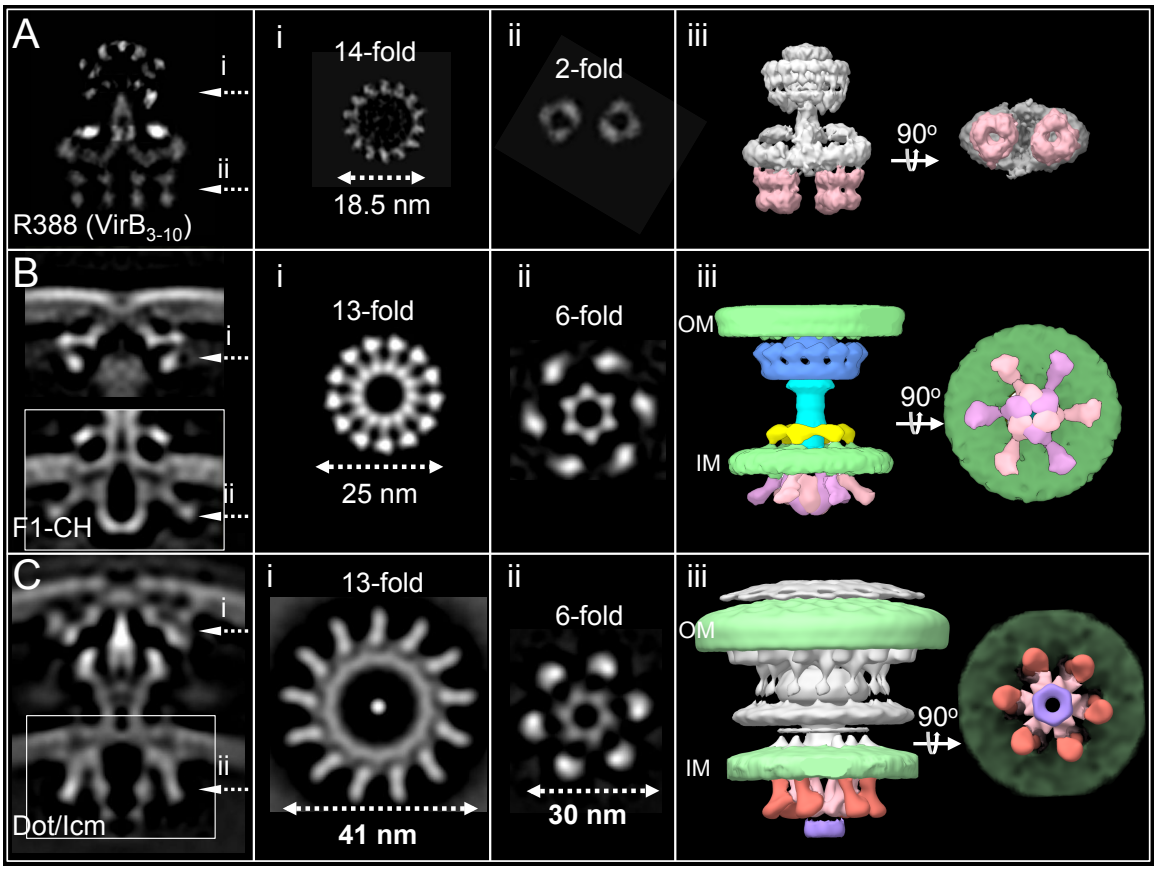

Fig. S8. Structural comparisons of the F-encoded F1-CH complex with other solved T4SSs. A-C) Central sections through longitudinal planes and cross-sections of the corresponding OMCs and IMCs of the $VirB_{3-10}$ substructure from the R388 conjugation machine, the F-encoded F1-CH complex, and the Dot/Icm T4SS. **A)** A central section of the $VirB_{3-10}$ substructure solved by negative-stain, single-particle reconstruction shows the barrel-shaped OMC and asymmetric IMC; **Ai-ii**, cross-sections at the positions indicated reveal the OMC 14-fold and IMC 2-fold symmetries; **Aiii**, surface rendering of the $VirB_{3-10}$ substructure highlighting the IMC with side-by-side hexamers of the VirB4 ATPase (pink-shaded). **Bi-iii**, corresponding images of the F-encoded F1-CH complex solved by *in situ* CryoET showing the 13-fold symmetric OMC and the 6-fold symmetric IMC marked by the hexamer of dimer arrangement of VirB4-like TraC (pink, dimer pairs are alternately shaded lighter and darker). **Ci-iii**, corresponding depictions of the Dot/Icm T4SS solved by *in situ* CryoET showing the 13-fold symmetric OMC and the 6-fold symmetric IMC marked by the hexamer of dimer arrangement of VirB4-like DotO (pink-shaded) and a hexamer of VirB11-like DotB (purple-shaded). White boxes indicate that the IMCs were refined separately from the OMCs.

Movie S1. 3-D visualization of a tomographic reconstruction and the intact F-encoded structures in *E. coli* minicells.

Movie S2. Structural changes accompanying transition of the quiescent F1-CH complex to the F-pilus generating F2-CH/Pilus complex.

REFERENCES

1. Sawitzke JA*, et al.* (2013) Recombineering: using drug cassettes to knock out genes in vivo. *Methods Enzymol* 533:79-102.
2. Farley MM, Hu B, Margolin W, Liu J (2016) Minicells, Back in fashion. *J Bacteriol* 198(8):1186-1195.
3. Gordon JE*, et al.* (2017) Use of chimeric type IV secretion systems to define contributions of outer membrane subassemblies for contact-dependent translocation. *Mol Microbiol* 105(2):273-293.
4. Mastronarde DN (2005) Automated electron microscope tomography using robust prediction of specimen movements. *J Struct Biol* 152(1):36-51.
5. Morado DR, Hu B, Liu J (2016) Using Tomoauto: A protocol for high-throughput automated cryo-electron tomography. *J Vis Exp* (107):e53608.
6. Li X*, et al.* (2013) Electron counting and beam-induced motion correction enable near-atomic-resolution single-particle cryo-EM. *Nat Methods* 10(6):584-590.
7. Kremer JR, Mastronarde DN, McIntosh JR (1996) Computer visualization of three-dimensional image data using IMOD. *J Struct Biol* 116(1):71-76.
8. Agulleiro JI, Fernandez JJ (2015) Tomo3D 2.0--exploitation of advanced vector extensions (AVX) for 3D reconstruction. *J Struct Biol* 189(2):147-152.
9. Hu B*, et al.* (2015) Visualization of the type III secretion sorting platform of *Shigella flexneri*. *Proc Natl Acad Sci U S A* 112(4):1047-1052.
10. Pettersen EF*, et al.* (2004) UCSF Chimera--a visualization system for exploratory research and analysis. *J Comp Chem* 25(13):1605-1612.
11. Vega DE, Margolin W (2018) Suppression of a thermosensitive *zipA* cell division mutant by altering amino acid metabolism. *J Bacteriol* 200(2). 200(2). pii: e00535-17. doi: 10.1128/JB.00535-17.
12. Li G, Young KD (2012) Isolation and identification of new inner membrane-associated proteins that localize to cell poles in *Escherichia coli*. *Mol Microbiol* 84(2):276-295.
13. Thomason LC, Sawitzke JA, Li X, Costantino N, Court DL (2014) Recombineering: genetic engineering in bacteria using homologous recombination. *Curr Protoc Mol Biol* 106:1 16 11-39.
14. Frost L, Ippen-Ihler K, Skurray R (1994) Analysis of the sequence and gene products of the transfer region of the F sex factor. *Microbiol Rev* 58:162-210.
15 Lu J*, et al.* (2002) Analysis and characterization of the IncFV plasmid pED208 transfer region. *Plasmid* 48(1):24-37.
16. Low HH*, et al.* (2014) Structure of a type IV secretion system. *Nature* 508(7497):550-553.
17. Chetrit D, Hu B, Christie PJ, Roy CR, & Liu J (2018) A unique cytoplasmic ATPase complex defines the *Legionella pneumophila* type IV secretion channel. *Nat Microbiol* 3(6):678-686.
18. Lawley TD, Klimke WA, Gubbins MJ, Frost LS (2003) F factor conjugation is a true type IV secretion system. *FEMS Microbiol Lett* 224(1):1-15.
19. Harris RL, Hombs V, Silverman PM (2001) Evidence that F-plasmid proteins TraV, TraK and TraB assemble into an envelope-spanning structure in Escherichia coli. *Mol Microbiol* 42(3):757-766.
20. Harris RL, Silverman PM (2004) Tra proteins characteristic of F-like type IV secretion systems constitute an interaction group by yeast two-hybrid analysis. *J Bacteriol* 186(16):5480-5485.
21. Cascales E, Christie PJ (2004) *Agrobacterium* VirB10, an ATP energy sensor required for type IV secretion. *Proc Natl Acad Sci U S A* 101(49):17228-17233.
22. Hu B, Lara-Tejero M, Kong Q, Galan JE, Liu J (2017) *In situ* molecular architecture of the Salmonella type III secretion machine. *Cell* 168(6):1065-1074 e1010.
23. Chang YW*, et al.* (2016) Architecture of the type IVa pilus machine. *Science* 351(6278):aad2001